ADVANCED ENGINEERING MATERIALS
www.aem-journal.com

Convolutional Neural Network-Based Regression Model for Distribution Data from X-Ray Radiographs of Metallic Foams

Tristan E. Kammbach, Paul H. Kamm, Tillmann R. Neu, and Francisco García-Moreno*

The difficult determination of morphological properties in metal foams stands behind the reasons why metal foams are not widely used in industry, since quality control of the batches produced is limited to destructive methods. To approach this challenge, a new method of analysis of morphological properties based on 2D X-Ray radiograms and the employment of a new Convolutional Neural Network architecture is proposed. The training of this model is based on a combined approach of simulating simplified foams as pretraining data and the acquisition of real experimental data, extracted from X-Ray computer tomographies. The network is trained successfully with 41 foams to obtain predictions for cell size distribution between 0.3 and 5 mm, as well as sphericities in ranges from 0.4 to 1. In addition, tests are carried out to get an insight into the robustness of the model when confronted with similar data that are not included in the training process. It is found that the effectiveness of the neural network increases with a larger number of cells in the observed volume where above 500 cells per volume 92.5% of sphericity predictions and 99.4% of cell size predictions passed the Kolmogorov-Smirnov test.

1. Introduction

Foams of various materials are widely used in lightweight industrial applications due to their specific properties.[1,2] Among these, metal foams offer good thermal and electrical conductivity as well as high specific strength and stiffness in addition to other properties such as high vibration damping and shock absorption capability. Hereby, aluminum foams are the most common type of metal foams for mechanical applications.[3–6] However, as finely structured materials, metal foams are also subject to a high sensitivity toward degradation from its large surface and have a poor resistance against tensile stresses. To remedy this and to improve their stiffness, metal foams are often employed as a foam sandwich, where a central core of foamed material is surrounded by a face sheet of bulk material as the top and bottom layer, providing the material with an increased toughness against tensile stresses and bending stiffness as well as providing a protection against corrosive attacks.[5,7–10] Further, the face sheets allow for a better welding or other types of joining techniques. Commonly used sandwich configurations consist of a core and two face sheets made of different aluminum alloys which are connected by a metallic bonding. This design is called aluminum foam sandwich (AFS). Due to their foam core, AFS quality is strongly dependent on a low dispersion in the cell size distribution,[11] specific density,[9] and the sphericity of the cells.[12] All these parameters can be measured with X-Ray computer tomography (XCT). However, during production, quality control of these features cannot be carried out nondestructively as the sample size is often simply too large[13] and XCT acquisition times are too long. Therefore, the available nondestructive methods with acquisition times in the seconds range must be improved to provide the aforementioned information. Amongst those methods 2D-X-Ray radiography proves as a promising candidate as it can capture the entire information as an integration of absorptions of all constituents in the path from the source to the detector at each pixel with resolutions in the micrometer range. A proper disentanglement of this superpositioned data should therefore be able to provide an insight into the features as mentioned above. For example, given a known attenuation coefficient, using the Lambert–Beer law, the specific density can be calculated. As Körner et al. have shown, the specific density is correlated with the mean cell diameter.[14] In contrast, the more complex distribution data is much harder to acquire. With the emergence of artificial intelligence, a new opportunity for data analysis became unlocked, where neural networks can be trained to reconstruct, characterize, or evaluate X-Ray radiographies to obtain the above-mentioned AFS descriptive parameters, if enough training data is provided. Deep learning neural networks have for example been employed to detect Covid-19 in tomographies[15] and X-Ray images.[16]

In cellular media many of the neural networks employed focus on the segmentation of images, attempting to supersede the

T. E. Kammbach, P. H. Kamm, T. R. Neu, F. García-Moreno
Institute of Applied Materials
Helmholtz-Zentrum Berlin für Materialien und Energie
Hahn-Meitner-Platz 1, 14109 Berlin, Germany
E-mail: tristan.kammbach@helmholtz-berlin.de,
t.kammbach@tu-berlin.de

T. E. Kammbach
Institute of Materials Science and Technology
Technische Universität Berlin
Hardenbergstr. 36, 10623 Berlin, Germany

The ORCID identification number(s) for the author(s) of this article can be found under https://doi.org/10.1002/adem.202401128.

© 2024 The Author(s). Advanced Engineering Materials published by Wiley-VCH GmbH. This is an open access article under the terms of the Creative Commons Attribution License, which permits use, distribution and reproduction in any medium, provided the original work is properly cited.

DOI: 10.1002/adem.202401128

computationally taxing conventional image analysis methods like the watershed algorithm or Otsu thresholding.[17–21] These segmentation approaches enable the user to then acquire the relevant cellular parameters from the volumetric data. It has been established that through the employment of a neural network it is feasible to acquire descriptive data from 2D images directly[22–26] while some approaches take a middle path by reconstructing a virtual 3D representation from orthographic projections where segmentations can be performed upon.[27,28] Transferring that knowledge, we therefore propose to train a neural network to quantify typically 3D parameters from two-dimensional radiographic images of the object of interest as created through X-Ray radiography. (comp. **Figure 1**)

2. Experimental Section

2.1. Experimental Data Acquisition and Augmentation

XCTs were carried out on 45 different metal foams, half of which were AFS. To provide training on a broad set of samples, the dimensions of the foams were widely varied and ranged from $20 \times 20 \times 15$ mm to $90 \times 150 \times 40$ mm pieces with the limiting constraints being the decreasing number of cells in the foams on the lower end and the size of the X-Ray detector on upper end. The tomographies were prepared in nine batches by hotgluing the aforementioned metal foams together, which allowed for a larger number of foams per batch as the low X-Ray absorption coefficient of the hot-glue made for an easy removal during the segmentation step. The specifics of the experimental setup can be viewed in **Table 1**.

The acquired projection images (**Figure 2**) were reconstructed with the software "Octopus reconstruction" (Inside Matters, version 8.8.2.7) and digitally cut and segmented via "Avizo" (Thermofischer, Germany, version 9.0.1), with a 3D resolution of 0.041 mm. During the cutting process the bulk plates of the AFS were digitally removed. Unsegmented volumes were saved alongside segmented ones for later use as projection radiograms. To augment the data subvolumes $V_{sub} = a^2 t$ were sliced from the volume V_0 of the cuboid foam tomograms $V_0 = a_0\ b_0\ c_0$; $a_0 \geq b_0 \geq c_0$. The dimensions a, t of the sliced subvolumes were set with a cut of the length $t \in [0.7c_0, c_0]$, made along the short side of the cuboid base volume and cuts of length $a \in [256\,\text{voxel}, b_0]$ made to the remaining two sides. Based on equal probabilities the slices were then rotated by multiples of 90° as well as mirrored. In this way, roughly 6600 distinct subvolumes were created from 41 volumes. The remaining four volumes where augmented into 850 subvolumes and set aside to test the final model with.

Table 1. Experimental parameters of the XCTs.

Category	Setting
Configuration	Cone Beam
X-ray source	Hamamatsu, Tungsten target, 100 kV, 500 µA
Detector	Flat panel, 50 × 50 µm per pixel
Distance: source-detector	900 mm
Distance: source-object	735 mm
Number of images	1001
Acquisition mode	Integral of four images
Acquisition time	4 × 500 ms
Rotation angle	360°
Field of view	2240 × 2368 pixel

2.2. Foam Simulation

In addition to the experimental data acquisition and augmentation, artificial foam volumes were created by performing a 3D Voronoi tessellation. Simulated foams produced this way, provided a good trade-off between computational costs and closeness to real, complex foam structures[29,30] and had in the context of grain size distributions already been successfully

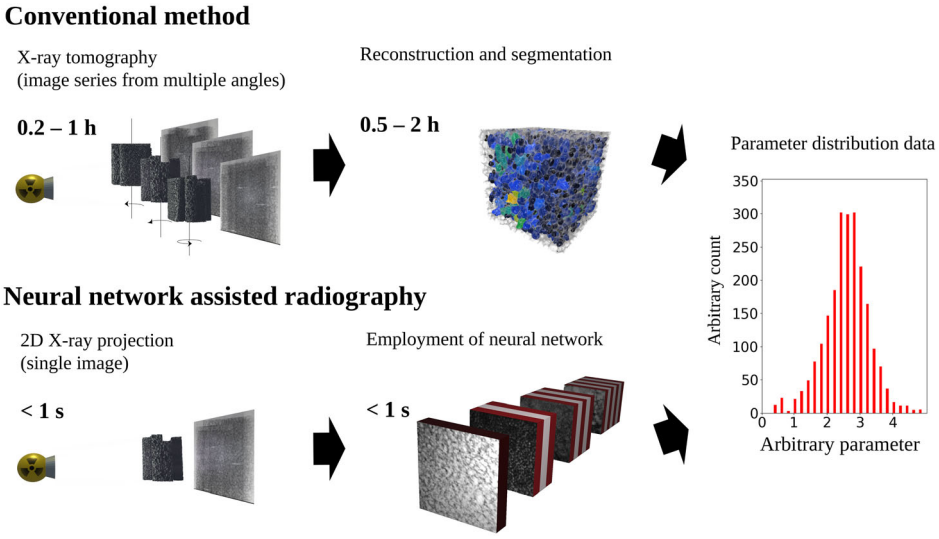

Figure 1. Comparison of the time frames between the conventional method to 3D parameter acquisition and the proposed method.

© 2024 The Author(s). Advanced Engineering Materials published by Wiley-VCH GmbH

15272648, 0, Downloaded from https://onlinelibrary.wiley.com/doi/10.1002/adem.202401128 by Technische Universitaet Berlin, Wiley Online Library on [21/11/2024]. See the Terms and Conditions (https://onlinelibrary.wiley.com/terms-and-conditions) on Wiley Online Library for rules of use; OA articles are governed by the applicable Creative Commons License

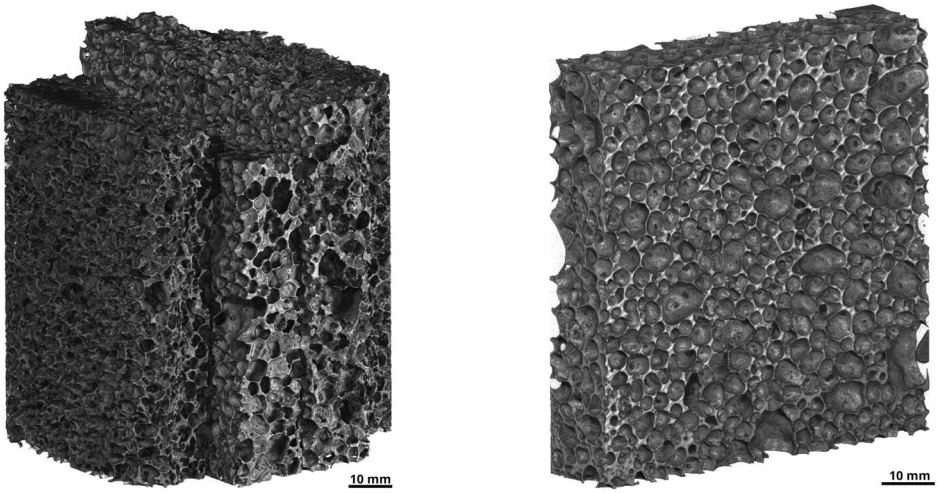

Figure 2. Examples of metal foams from reconstructed tomograms. Left: Stack of images as prepared for the image acquisition. Right: Singular metal foam from the stack.

employed for the training of neural networks.[31] To improve the visual similarity to real wet foams like metal foams, the Voronoi foams were then modified by consecutive use of a median and Gauss filter to blur and therefore widen the 1 pixel thick cell wall and a threshold filter to re-binarize image. This was followed by an iterative process by which cells were reshaped by increasing the number of voxels closer to the vertices and the initial Voronoi grid based on the number of already present neighboring voxels. Simulated volumes were then segmented using a watershed algorithm. Randomly varying the parameters of the Voronoi tessellation and the subsequent filters yielded 5000 distinct volumes for further processing pretraining data, close to doubling the amount of information the network was fed during the training process.

2.3. Dataset Handling

As the target data was a quantitative parameter distribution (histogram) of all the cells in the volume. (compare **Figure** 3), corresponding pairs of input images and output histograms (also referred to as expected data or expected distribution) were created to train and test the model. Therefore, for each volume the contained cells were analyzed in terms of cell volume and anisotropy. To prevent division-by-zero errors during the later principal component analysis (PCA) cells below a size of seven voxels were discarded as artifacts. Additionally, only cells fully contained within the volume were analyzed. To quantify the cell volume, the number of voxels per each cell N_{voxel} was acquired and multiplied with the volume of a singular voxel V_{voxel}. An equivalent diameter D was then calculated from that volume under the assumption of each cell being perfectly spherical.

$$D = \sqrt[3]{\frac{6}{\pi} V_{\text{voxel}} N_{\text{voxel}}} \tag{1}$$

The quantification of the anisotropy was performed by calculating the WADELL sphericity Ψ per each cell via a PCA of the positional data for each voxel within.[32,33] The square root of the eigenvalues $[\lambda_1, \lambda_2, \lambda_3]$ of the voxels for a PCA of each cell were equivalent to the lengths of the axis of an ellipsoid that is enclosed the cell. Based on that, the WADELL sphericity was calculated as follows

$$\Psi = \sqrt[3]{\frac{\lambda_3}{\sqrt{\lambda_1 \lambda_2}}}, \quad \text{with} \quad \lambda_1 \leq \lambda_2 \leq \lambda_3 \tag{2}$$

For the sphericity as well as for the cell diameter the data was then compiled into histograms for each volume by summing up the counts of cells with parameters values within specific intervals. The bin count n_{bin}, interval I_{bin} and width d_{bin} were chosen to best reflect the dataset as shown in **Table 2**. After a rescaling ($x_{\min} = 0$, $x_{\max} = \max(\text{all histograms})$), these histograms that made up the output data the model were trained on and evaluated (Figure 3, Output).

Equally, following a rescaling, the image scales and the thicknesses per each subvolume were stored as metadata (Figure 3, Input 2). Then the images used as input values were created by a projection in thickness direction of the segmented volumetric data for the Voronoi tessellation and the unsegmented slices of tomograms for the experimentally acquired data. The projections were then reduced in dimensions to a size of 256×256 pixel (Figure 3, Input 1). The data was randomly cut into three sets of the according proportions: 70% training, 20% test, 10% evaluation. This served to retain a sub-set of data that was entirely unknown to the trained neural network. The sets for the sphericity and cell size distribution model were individually randomized. To summarize the scope of the training data and as such the resulting model the training data was encapsulated within the following parameter: The real length of the square projection images was between 10 and 80 mm while the depth projected toward, ranged from 7 to 75 mm. Only projections exclusively containing cells were utilized and therefore no partial images. The cell sizes ranged from 0.3 to 5 mm and the distributions

© 2024 The Author(s). Advanced Engineering Materials published by Wiley-VCH GmbH

15272648, 0, Downloaded from https://onlinelibrary.wiley.com/doi/10.1002/adem.202401128 by Technische Universitaet Berlin, Wiley Online Library on [21/11/2024]. See the Terms and Conditions (https://onlinelibrary.wiley.com/terms-and-conditions) on Wiley Online Library for rules of use; OA articles are governed by the applicable Creative Commons License

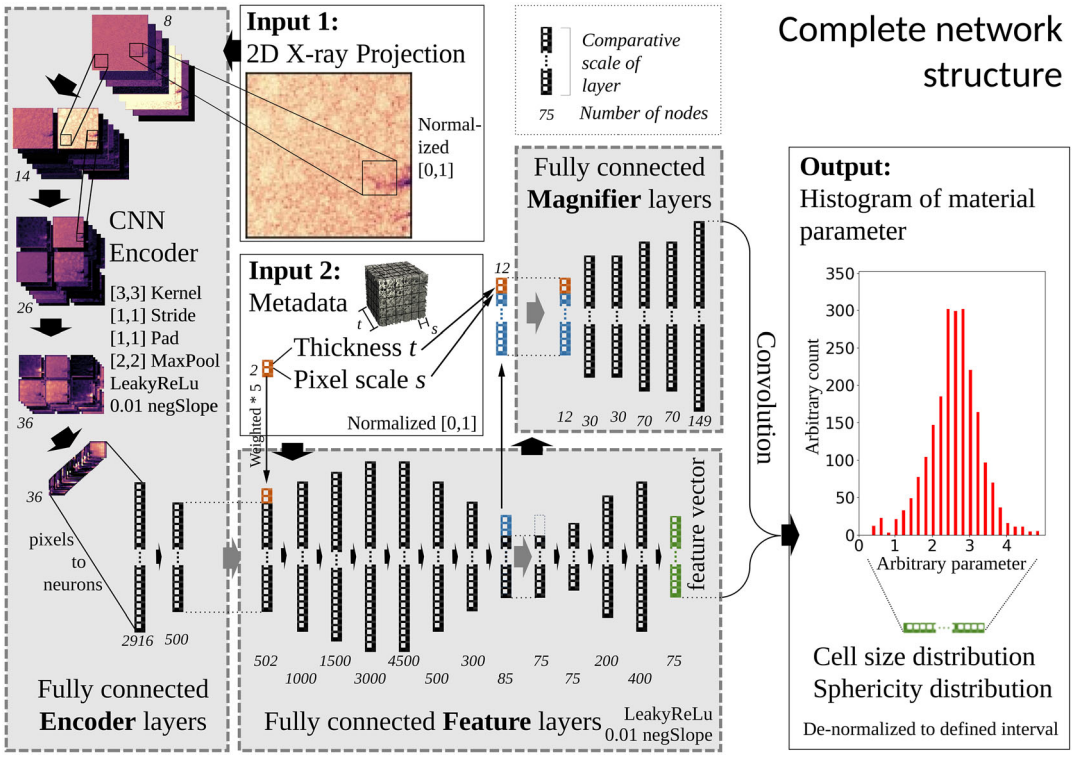

Figure 3. Structure of the employed network. After encoding the image information, the pixel scale and thickness of the original volume are injected as a secondary input. This provides the network with sufficient information to predict the distribution of 3D parameters.

Table 2. Binning parameters for distribution datasets.

	n_{bin}	I_{bin}	d_{bin}
Cell size distribution	75	[0, 5]mm	$\frac{1}{15}$ mm
Sphericity distribution	30	[0, 1]	$\frac{1}{30}$

of the sphericities of about 0.4–1, which did not diverge from those usually found in metal foams.

2.4. Network Architecture

The network consisted of three major segments, namely the *Encoder*, the *Feature layer* and the *Magnifier layer* (see Figure 3). The core of the neural network was the *Feature layer* or *Feature MLP* (*Multilayer perceptron*) and was made up of several fully connected layers. The *Feature layer* takes the encoded image and metadata and precomputes them into a vector, containing encoded information of the relative distribution data (*Feature vector*). The *Feature MLP* requires 2 types of input: 1) the previously mentioned metadata comprising of normalized scale and thickness information and 2) an encoded version of the projection image. The encoding of the projection image was carried out by a separately trained *Encoder*. Its purpose was to reduce the input dimensions of the projection image from 256×256 pixel (65 536 8-bit float values), to a more manageable encoded vector of 500 values, reducing it by a factor of about 131. This was achieved by training an *Autoencoder* on reproducing the input data and then using the *Encoder* section. This approach greatly improved training times and consistency. To correct the data in shift and scale, the *Feature layers* output was further enhanced through the employment of another branch of the deep learning network, the *Magnifier*. The convolution of its output with the padded output of the *Feature MLP* produced a rectified prediction of the distribution data in question. The *Magnifier* was a small, fully connected, deep network of which the inputs consisting of the metadata and ten values split from a bottlenecked section of the *Feature MLP*. To perform the final convolution, the size of the *Magnifiers* output vector was bound to the length m of output vector X of the *Feature MLP* with $X \in \mathbb{R}^m$. Accordingly, the *Magnifiers* output is a vector M of the following dimensions: $M \in \mathbb{R}^y, n = 2(m-1)+1$. To result in a convolution without a loss in length, the Feature vector X must be padded with zeros to the new dimensions $X_{pad} \in \mathbb{R}^{3m-2}$. While the *(Auto-)Encoder* was trained separately on the input–input dataset, the *Feature MLP* and *Magnifier* were trained together on the input–output datasets.

The resulting output was a vector of the normalized absolute counts per each bin in the histogram (modified feature vector). For the loss function the mean square error function was used. In the case of the *Autoencoder* this compared normalized pixel values of the input and the decoded output image and sumed up the difference over all the pixels of the images. The loss function used for the distribution data was a slightly modified version of the mean square error function which allocated a small

© 2024 The Author(s). Advanced Engineering Materials published by Wiley-VCH GmbH

15272648, 0, Downloaded from https://onlinelibrary.wiley.com/doi/10.1002/adem.202401128 by Technische Universitaet Berlin, Wiley Online Library on [21/11/2024]. See the Terms and Conditions (https://onlinelibrary.wiley.com/terms-and-conditions) on Wiley Online Library for rules of use; OA articles are governed by the applicable Creative Commons License

additional loss for larger variances between the error values of neighbouring vector components, resulting in more uniform distributions. The network was created in Python using PyTorch under the use of the Adam optimizer.[34] The activation function for each neuron was LeakyReLU[35] which proved particularly useful in improving the training effectiveness of the *Autoencoder* where "dying" neurons where a significant issue before when using standard ReLU. The number of neurons per each layer can be found in Figure 3, represented through the number in italics next to each layer. Every training was conducted with a batch size of 5.

2.5. Training Process

Three different training steps were performed to train the final network on one type of regression. As shown in **Figure 4**a, the initial step concerned the training of the *Autoencoder*. For this purpose the *Autoencoder* was subjected to a combined data set of simulated and experimentally acquired images. The training was conducted until convergence was achieved. With the *Encoder* in place the remainder of the network was first subjected to pretraining on simulated projection images. This training batch was run for different sets of hyperparameters until a regression model was found that would produce precise results for most simulated projections. The quality of the model was then pre-evaluated by three statistic metrics: 1) Plotting the average diameter or sphericity of modeled histograms from test data over the expected data. 2) Plotting the summed-up cell volumes of modeled and real data against each other. In case of the sphericity, the fraction value was summed up. In both cases, this allowed for a quick insight into how well the model predicted the total number of counts per bin. 3) Testing for passing the Kolmogorov–Smirnov test (KS test) between test and training data such, that the resulting prediction distribution $p_{\text{predicted}}$ can be considered to be of the same ground truth as the expected distribution p_{expected} (By rejecting the null hypothesis H_0 if its probability P is less than α. $H_0 : p_{\text{predicted}} \neq p_{\text{expected}}; \alpha = 0.05; P(H|0) < \alpha$).[36,37]

The best pretrained model was then used in the main training which was conducted on experimentally acquired specimens. Pretraining on the simulated data yielded a tangible decrease in training epochs and a lower initial and final loss for the proceeding main training compared to conducting the main training

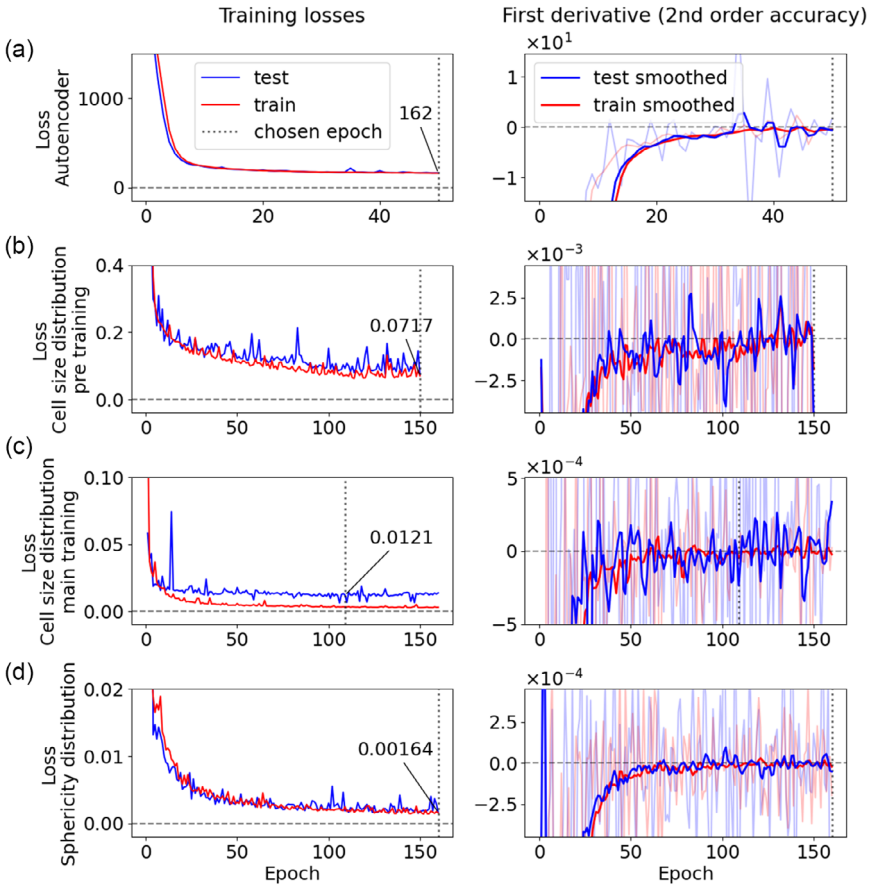

Figure 4. Loss convergence of the model trainings. a) After an initial training of the *Autoencoder*, the *Encoder* section of it was then plugged into the model. b,c) The resulting network architecture was then trained to predict the cell size distribution and d) cell sphericity distribution. To improve efficiency, the training for the prediction of the pore size distribution was performed in two steps where the network was pretrained on simulated foam data and then finished on experimental data. The training was halted at the epoch represented by the dotted line, when the training loss would no longer decrease. The column on the right side shows the smoothed derivative of the loss evolution, enhancing the point of diminishing returns. The annotated value corresponds to the loss value of the test data rounded to the third significant digit.

© 2024 The Author(s). Advanced Engineering Materials published by Wiley-VCH GmbH

15272648, 0, Downloaded from https://onlinelibrary.wiley.com/doi/10.1002/adem.202401128 by Technische Universitaet Berlin, Wiley Online Library on [21/11/2024]. See the Terms and Conditions (https://onlinelibrary.wiley.com/terms-and-conditions) on Wiley Online Library for rules of use; OA articles are governed by the applicable Creative Commons License

on an empty model. This final training was evaluated by the same means as pretraining to sieve out the best performing networks which were then subjected to a more thorough evaluation. Due to the difference of the sphericities featured by Voronoi foams and real foams, the pretraining for the sphericity distribution was omitted. The loss convergence of the chosen foams is displayed in Figure 4b–d. The main training of the cell size distribution (Figure 4b) was halted at an earlier point to avoid overfitting.

2.6. Distribution Prediction

After the main training was completed, the resulting model was able to predict the distribution of cell sphericities and cell sizes to varying degrees. **Figure 5** shows three examples of predictions that were taken from the common images in the evaluation data set of both models. As visible in Figure 5a, the model was capable of achieving a good match to the real data as gained from the segmentation. This was true even for more complex situations, as shown in Figure 5b, where a compression had caused an area of collapsed cells (darker region). However, there were some projections that where challenging for the model to predict like the projection shown in Figure 5c.

3. Discussion

3.1. Model Evaluation

To evaluate the model, the validation data set is subjected to the final model. To measure the goodness of fit in addition to the KS-test the residuals are calculated as a difference between modeled values and expected values per each bin. The standard deviations SD of all relative residuals r per prediction are used as a measure for model precision. With $y_y^\star$ being the modeled value, y_n the expected value, and $n_{\text{bin}} = n$ as the number of bins, it is calculated as follows

$$r_{n,\text{rel}} = \frac{y_n}{\sum y_n} - \frac{y_n^\star}{\sum y_n^\star}, \bar{r}_{n,\text{rel}} = \frac{1}{y}\sum^{y} r_{n,\text{rel}},$$
$$SD_{r,\text{rel}} = \sqrt{\frac{1}{n-1}\sum^{y}(r_{n,\text{rel}} - \bar{r}_{n,\text{rel}})^2} \tag{3}$$

Model accuracy is evaluated through the mean absolute scaled error (MASE), a measure often involved when different scales of data are to be compared.[38,39] Using the mean expected value $\bar{y}$ as base prediction, the error is calculated as such

$$\text{MASE} = \frac{1}{y}\frac{\sum^{n}|y_n - y_n^\star|}{\sum^{n}|\bar{y} - y_n|} \tag{4}$$

Using the summed-up predicted values (Figure 5d) as an indicator, a higher number of cells appears to correlate with increasingly better predictions. Plotting the test criteria over the number of cells which are fully included in the input projection image reveals that the goodness-of-fit increases with the cell count as shown in **Figure 6**. This is evident in the decreasing MASE (Figure 6a,d) and standard deviation of the residuals (Figure 6b,e) that asymptotically approach a lower boundary of below 1 and 0.01 respectively. This coincides with an increased ratio of pass-to-fail for the KS-test up to 1 for larger numbers of cells in the projection image (Figure 6c,f). Consistent matches between model and reality are achieved above a cell count per image of 500 for cell size distributions and 300 for the sphericity distribution. In total 42% of predictions passed the KS-test for the cell size distribution model. However, the percentage increased to 87.4% for images with more than 500 complete cells in the image. 92.5% passed the KS-test for the sphericity model increasing to 99.4% above 500 cells per projection image.

3.2. Behavior Toward Unfamiliar Data Sets

Testing the neural network on unfamiliar data sets reveals that the general trend repeats itself. **Figure 7**b shows the decrease in standard deviation for the cell size distribution in four unfamiliar foams. The plot reveals a general trend toward an increasing precision with higher cell counts. However, not all foams produce results well below the 0.01 threshold for sphericity distribution and the amount of passes for the KS test is considerably lower than before. For three of the four tested foams, the MASE mostly stays below 1 (compare Figure 7a). The graph does not show an obvious trend towards reduction with higher numbers of cells per projection. As the *Encoder* has only been trained on the initial data set the loss of the *Autoencoder* was reevaluated for the unfamiliar foam in Figure 7c. As apparent, the losses are on the same magnitude as the one from the initial image (compare Figure 4). This notion is reinforced by the similarity of features between the encoded (Figure 7b) and the decoded images (Figure 7c).

3.3. Evaluation of Model Performance

The network structure that was proposed in the frame of this work has proven the capability to reconstruct data of morphological properties in metal foams, that can commonly only be acquired through tomographic methods. The latter involve reconstructing a 3D virtual representation, from projection images of porous media such as AFS. In this context, a number of key features and general limitations in the networks capabilities have become evident.

The presented metrics for network evaluation strongly suggests a connection between the number of cells contained within the image and the precision and accuracy of the prediction. This has two explanations, the first being that for the model training partially contained cells were omitted. As those make up a much larger portion of the projected volume if the total number of cells is lower, the network is trained with naturally flawed data. In extreme cases this leads to images where the relevant information (complete cells) is located in less than half the pixels. The network would have to learn to mask the irrelevant information, a task that the core of the network, the *Feature layer* as a fully connected layer, is ill suited to and the *Encoder* has not been trained for. However, expanding the *Encoders* capabilities or training a separate network to mask incomplete cells is within the bounds of the achievable.

The second reason why images with a lower cell count perform worse is that the resulting histogram does not contain a

© 2024 The Author(s). Advanced Engineering Materials published by Wiley-VCH GmbH

15272648, 0, Downloaded from https://onlinelibrary.wiley.com/doi/10.1002/adem.202401128 by Technische Universitaet Berlin, Wiley Online Library on [21/11/2024]. See the Terms and Conditions (https://onlinelibrary.wiley.com/terms-and-conditions) on Wiley Online Library for rules of use; OA articles are governed by the applicable Creative Commons License

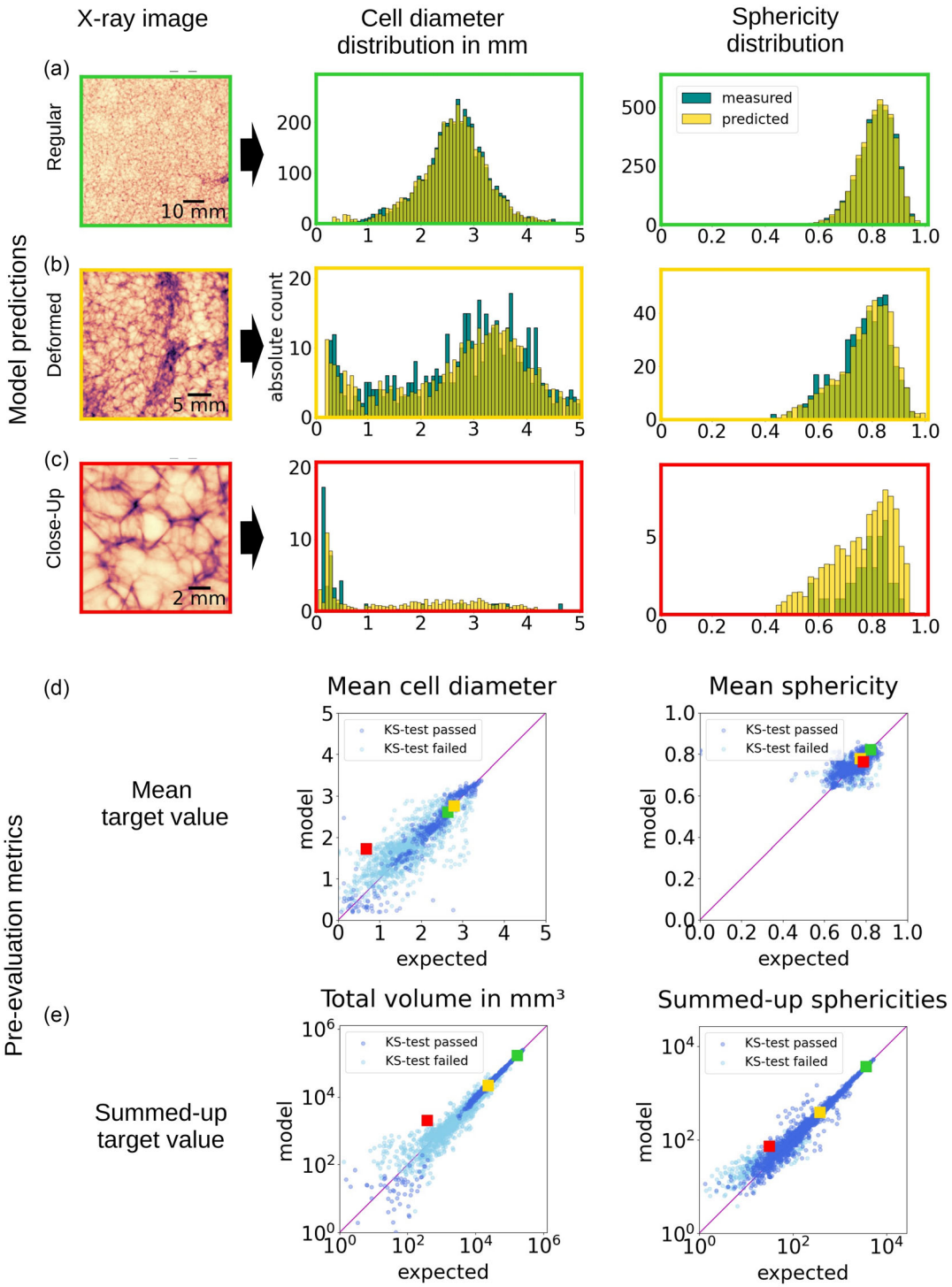

Figure 5. Summary of prediction results for the presented models. a–c) depict selected projections as representations for different cases. In the corresponding row, the measured parameter distributions (blue) are plotted overlapping with the model-based predictions (yellow) from the projections for cell size and sphericity. The overlap between the measured and predicted distributions is marked in green. d,e) contain the pre-evaluation metrics employed for the initial model evaluation in each row corresponding to the target parameter the model was trained for. The red, yellow and green squares within the plots correspond to the colour coding of the frames for the projections in (a–c).

© 2024 The Author(s). Advanced Engineering Materials published by Wiley-VCH GmbH

15272648, 0, Downloaded from https://onlinelibrary.wiley.com/doi/10.1002/adem.202401128 by Technische Universitaet Berlin, Wiley Online Library on [21/11/2024]. See the Terms and Conditions (https://onlinelibrary.wiley.com/terms-and-conditions) on Wiley Online Library for rules of use; OA articles are governed by the applicable Creative Commons License

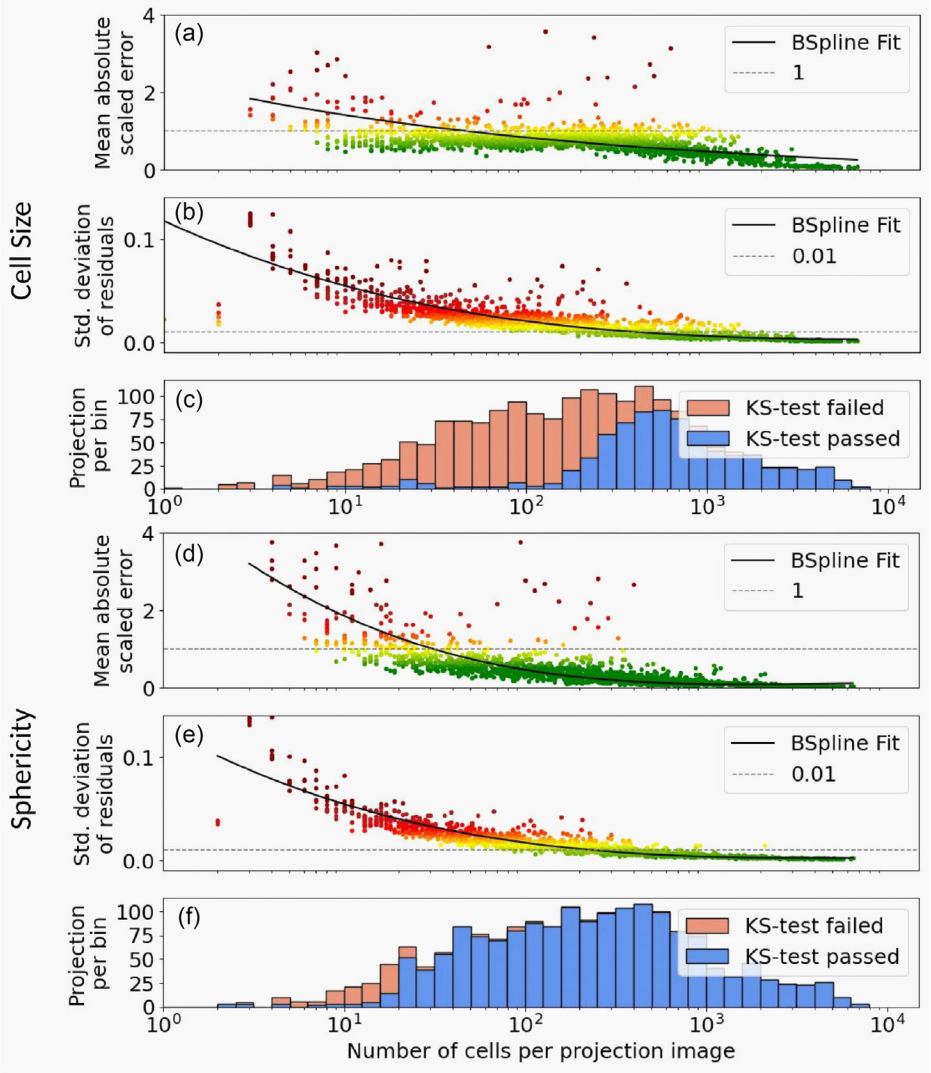

Figure 6. MASE, standard deviation of residuals and KS-test results over the number of cells per projection image on a log10 scale for cell size (a–c) and sphericity (d–f). Bin widths for plot (c) and (f) were adjusted to the logarithmic scale. Due to the nature of logarithmic scales, zero-value results (images without any full cells) have been filtered from the data. To reflect the assumption of a lower limit for infinitely high cell numbers, B-Spline curves have been virtually padded with rightmost value.

statistical distribution of cells as it would in larger volume projections. In contrast, the network structure appears to be more capable of predicting the statistical distribution of the cellular media it is subjected to. Within the limits of a thickness of at maximum 90 mm that the experimental X-Ray setup provided, increasing the projected volume would not produce any adverse effects. However, the trend of the *encoder–decoder* loss (Figure 7c) hints at a limit for prediction quality improvements as the information per pixel increases too much for the *Encoder* to handle.

Overall, the network performs much better for sphericity distribution predictions. This can be explained by there being less variety between the shapes of distributions within the training data set. The range of possible modes the network had to learn was smaller, making loss convergence easier and the model more precise.

When subjected to unfamiliar foams of the same family as the model was trained with, precision and accuracy are lower. The implicit prediction of the cell number, necessary for a high accuracy, does not persist as previously seen with the evaluation data set. Conversely, the precision does still improve with the number of cells. Overall, the network structure is transferable to previously unknown data of comparable foams and able to generate predictions with a high goodness of fit. However, metal foams feature a great diversity of structures which are often made more complex by factors like spatial gradients in cell size and sphericity, defects such as abnormally large cells, mechanically collapsed regions or sections of bulk material where the foaming did not set in.[40] Due to the limited scope of this work not all of these cases have been included in the training set. Therefore, it is to be expected that the quality of the model will increase with a larger

© 2024 The Author(s). Advanced Engineering Materials published by Wiley-VCH GmbH

15272648, 0, Downloaded from https://onlinelibrary.wiley.com/doi/10.1002/adem.202401128 by Technische Universitaet Berlin, Wiley Online Library on [21/11/2024]. See the Terms and Conditions (https://onlinelibrary.wiley.com/terms-and-conditions) on Wiley Online Library for rules of use; OA articles are governed by the applicable Creative Commons License

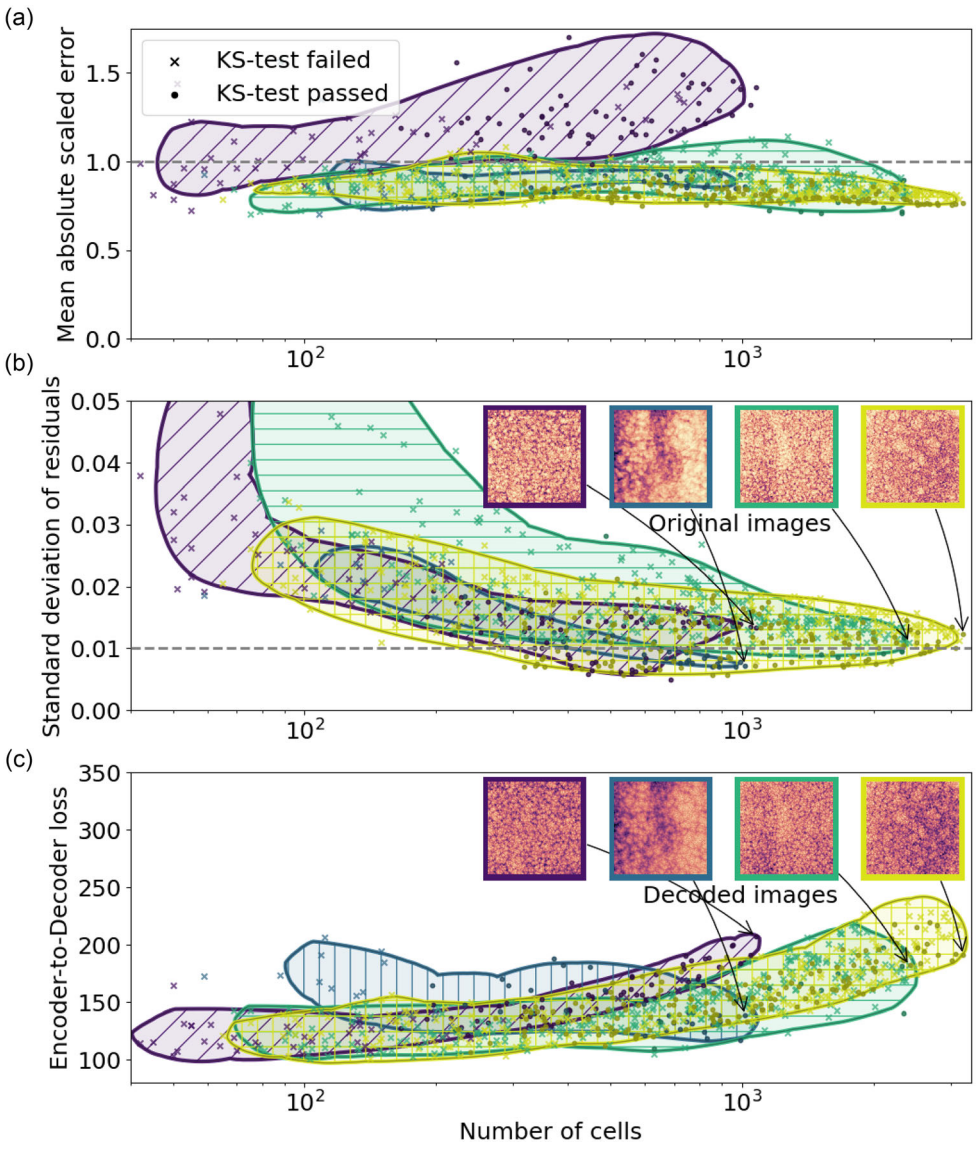

Figure 7. a) MASE, standard deviation of residuals for the prediction of the cell size distribution and encoder-to-decoder loss plotted against the number of cells per image. The highlighted areas show a smoothed concave hull of each foams point cloud, serving as an approximate, visual representation of its extend. The foams these prediction were done for were yet unknown to the neural network. b) depict the image corresponding to the largest number of cells for each of the four foams. c) Matching decoded images are shown. A low encoder-to-decoder loss indicates that the Autoencoder performs as expected for the unfamiliar foams.

data set to train upon as generally discussed by Halevy et al.[41] In this case, the inclusion of these different cellular structures in the training sets, featuring other distribution functions, will expand the models prediction capabilities.

4. Conclusion

In this article a novel approach to characterizing material parameters in metal foams has been presented. The network was trained on simulated Voronoi foams and 41 XCTs of real metallic foams. The foam data was subjected to an augmentation, which resulted in a data set of 5000 simulated and 6600 experimental X-Ray radiographic foam images. The training was aimed at the regression of the cell size distribution and the sphericity distribution from these images. A model evaluation was carried out on an augmented data set taken from the initial 41 foams and on another set taken from four unrelated foams of similar structure. It showed that a neural network based on the presented architecture was capable of predicting the cell size distribution and the sphericity distribution of cellular media like metallic foams for X-Ray images containing over 500 fully enclosed cells. The accuracy and precision are closely tied to the number of cells where high numbers produce results of a quality comparable to traditional segmentation-based approaches of 3D XCT for determining the parameter distribution. As mentioned by Zhou et al.[21]

© 2024 The Author(s). Advanced Engineering Materials published by Wiley-VCH GmbH

15272648, 0, Downloaded from https://onlinelibrary.wiley.com/doi/10.1002/adem.202401128 by Technische Universitaet Berlin, Wiley Online Library on [21/11/2024]. See the Terms and Conditions (https://onlinelibrary.wiley.com/terms-and-conditions) on Wiley Online Library for rules of use; OA articles are governed by the applicable Creative Commons License

the key improvements in using a neural network for distribution regressions lie in the much reduced preparation time and educational requirements as compared to alternative options. In addition to this, the presented method allows for a fast in-line application in quality control for industrial settings without interrupting the production process. Additionally, the application is not necessarily limited to metallic foams, but rather can be adapted to other cellular media as required.

Acknowledgements

The authors gratefully acknowledge financial support through the HZG Projekt "Avanti" (ZT-I-PF-4-035). The authors would like to thank Dr W.H. Seeliger from the company "Metalfoam" for kindly providing samples.

Open Access funding enabled and organized by Projekt DEAL.

Conflict of Interest

The authors declare no conflict of interest.

Author Contributions

Tristan Eric Kammbach: Conceptualization: (supporting); Data curation: (equal); Formal analysis: (lead); Investigation: (lead); Methodology: (lead); Resources: (equal); Software: (lead); Validation: (lead); Visualization: (lead); Writing—original draft: (lead); Writing—review & editing: (lead). **Paul Hans Kamm**: Conceptualization: (lead); Data curation: (equal); Investigation: (supporting); Methodology: (supporting); Resources: (supporting); Supervision: (equal); Writing—review & editing: (equal). **Tillmann Robert Neu**: Conceptualization: (supporting); Data curation: (supporting); Resources: (supporting); Validation: (supporting); Writing—review & editing: (equal). **Francisco Garcia-Moreno**: Conceptualization: (equal); Funding acquisition: (lead); Project administration: (lead); Resources: (lead); Supervision: (lead); Validation: (supporting); Writing—review & editing: (equal).

Data Availability Statement

The data that support the findings of this study are available from the corresponding author upon reasonable request.

Keywords

image processing, metal foam, neural network, X-ray radiography, X-ray tomography

Received: May 10, 2024
Revised: October 2, 2024
Published online:

[1] M. F. Ashby, T. Evans, N. A. Fleck, J. W. Hutchinson, H. N. G. Wadley, L. J. Gibson, in *Metal Foams: A Design Guide*, Elsevier, Amsterdam **2000**.
[2] M. F. Lorna, J. Gibson, in *Cellular Solids - Structure and Properties*, University Press, Cambridge **1997**.
[3] J. Banhart, in *Conf. on Metal Foams and Porous Metal Structures* (Eds: J. Banhart, M. Ashby, N. Fleck) Vol. *14*, MIT Publ., Bremen, Germany **1999**, Ch. 16.
[4] A. Jafarizadeh, M. Ahmadzadeh, S. Mahmoudzadeh, M. Panjepour, *Transp. Porous Media* **2023**, *147*, 59.
[5] A. Kulshreshtha, S. K. Dhakad, *Mater. Today: Proc.* **2020**, *26*, 1784.
[6] M. Mahadev, C. G. Sreenivasa, K. M. Shivakumar, *IOP Conf. Ser.: Mater. Sci. Eng.* **2018**, *376*, 012081.
[7] J. Banhart, F. García-Moreno, K. Heim, H.-W. Seeliger, in *Light Weighting for Defense, Aerospace, and Transportation, Vol. 1 of Indian Institute of Metals Series* (Eds: A. A. Gokhale, N. E. Prasad, B. Basu), Springer, Singapore **2019**, pp. 61–72.
[8] S. Alexander, *Ph.D. Thesis*, Brandenburgische Technische Universität (Cottbus-Senftenberg), Germany **2011**.
[9] F. García-Moreno, *Materials* **2016**, *9*, 85.
[10] H.-W. Seeliger, *Adv. Eng. Mater.* **2004**, *6*, 448.
[11] E. Mancini, F. Campana, D. Pilone, M. Sasso, *Procedia Manuf.* **2020**, *47*, 1490.
[12] A. Jung, S. Diebels, *Adv. Eng. Mater.* **2019**, *21*, 1900237.
[13] J. Banhart, *Prog. Mater. Sci.* **2001**, *46*, 559.
[14] C. Körner, M. Arnold, R. F. Singer, *Mater. Sci. Eng., A* **2005**, *396*, 28.
[15] M. Polsinelli, L. Cinque, G. Placidi, *Pattern Recognit. Lett.* **2020**, *140*, 95.
[16] T. Ozturk, M. Talo, E. A. Yildirim, U. B. Baloglu, O. Yildirim, U. R. Acharya, *Comput. Biol. Med.* **2020**, *121*, 103792.
[17] N. J. Alqahtani, Y. Niu, Y. D. Wang, T. Chung, Z. Lanetc, A. Zhuravljov, R. T. Armstrong, P. Mostaghimi, *Transp. Porous Media* **2022**, *143*, 1.
[18] I. Ar Rushood, N. Alqahtani, Y. D. Wang, M. Shabaninejad, R. Armstrong, P. Mostaghimi, in *SPE Annual Technical Conf. and Exhibition*, OnePetro, Virtual **2020**.
[19] C. Gobert, A. Kudzal, J. Sietins, C. Mock, J. Sun, B. McWilliams, *Addit. Manuf.* **2020**, *36*, 101460.
[20] Y. D. Wang, M. J. Blunt, R. T. Armstrong, P. Mostaghimi, *Earth-Sci. Rev.* **2021**, *215*, 103555.
[21] S. Zhou, W. Sheng, Z. Wang, W. Yao, H. Huang, Y. Wei, R. Li, *Constr. Build. Mater.* **2019**, *208*, 144.
[22] K. Venkateshwar, S. H. Tasnim, S. A. Gadsden, S. Mahmud, *J. Energy Storage* **2022**, *51*, 104386.
[23] F. Kolodziejczyk, B. Mortazavi, T. Rabczuk, X. Zhuang, *Int. J. Heat Mass Transfer* **2021**, *172*, 121119.
[24] J. Sun, Y. Xu, L. Wang, *Metals* **2023**, *13*, 284.
[25] Y. Hangai, S. Ozawa, K. Okada, Y. Tanaka, K. Amagai, R. Suzuki, *Materials* **2023**, *16*, 1894.
[26] J. Torre, S. Barroso-Solares, M. A. Rodríguez-Pérez, J. Pinto, *Polymer* **2024**, *291*, 126597.
[27] F. Zhang, X. He, Q. Teng, X. Wu, X. Dong, *J. Petrol. Sci. Eng.* **2022**, *208*, 109652.
[28] J. Feng, Q. Teng, X. He, L. Qing, Y. Li, *Comput. Mater. Sci.* **2018**, *144*, 181.
[29] X. Zhang, Y. Wu, L. Tang, Z. Liu, Z. Jiang, Y. Liu, H. Xi, *Mech. Adv. Mater. Struct.* **2018**, *25*, 1265.
[30] Y. Duan, B. Du, X. Zhao, N. Hou, X. Shi, B. Hou, Y. Li, *Int. J. Mech. Sci.* **2019**, *164*, 105151.
[31] M. K. Padhan, A. Rai, M. Mitra, *Comput. Mater. Sci.* **2023**, *229*, 112416.
[32] H. Wadell, *J. Geol.* **1933**, *41*, 310.
[33] W. C. Krumbein, *J. Sediment. Res.* **1941**, *11*, 6472.
[34] D. P. Kingma, J. Ba, presented at *3rd ICLR*, San Diego, January **2017**, Ch. d.
[35] A. L. Maas, A. Y. Hannun, A. Y. Ng, *J. Mach. Learn. Res.* **2013**, *28, https://api.semanticscholar.org/CorpusID:16489696*.
[36] A. N. Kolmogorov, *Giorn Dell'inst Ital Degli Att* **1933**, *4*, 89.
[37] N. V. Smirnov, *Bull. Math. Univ. Moscou* **1939**, *2*, 3.
[38] Y. Tang, L. Shang, R. Zhang, J. Li, H. Fu, *Eng. Appl. Artif. Intell.* **2024**, *129*, 107662.
[39] P. H. Franses, *Int. J. Forecast.* **2016**, *32*, 20.
[40] T. R. Neu, P. H. Kamm, N. von der Eltz, H.-W. Seeliger, J. Banhart, F. García-Moreno, *Mater. Sci. Eng., A* **2021**, *800*, 140260.
[41] A. Halevy, P. Norvig, F. Pereira, *IEEE Intell. Syst.* **2009**, *24*, 2 8.

 © 2024 The Author(s). Advanced Engineering Materials published by Wiley-VCH GmbH

15272648, 0, Downloaded from https://onlinelibrary.wiley.com/doi/10.1002/adem.202401128 by Technische Universitaet Berlin, Wiley Online Library on [21/11/2024]. See the Terms and Conditions (https://onlinelibrary.wiley.com/terms-and-conditions) on Wiley Online Library for rules of use; OA articles are governed by the applicable Creative Commons License